Investigation into the microstructure and dynamic compressive properties of selective laser melted Ti-6Al-4V alloy with different heating treatments

Yang Liu [1, 2, 3*], Huaizhong Xu [1], Lei Zhu [1], Xiaofeng Wang [1, 2], Quanquan Han [3, 4], Shuxin Li [1], Yonggang Wang [1, 2*], Rossitza Setchi [3], Di Wang [5*]

[1] Faculty of Mechanical Engineering & Mechanics, Ningbo University, Ningbo, 315211, China

[2] Key Laboratory of Impact and Safety Engineering, Ministry of Education, Ningbo University, Ningbo, 315211,China

[3] Cardiff School of Engineering, Cardiff University, Cardiff, CF243AA, UK

[4] School of Mechanical Engineering, Shandong University, Jinan, 250061, China

[5] School of Mechanical and Automotive Engineering, South China University of Technology, Guangzhou 510640, China

Abstract: As a commonly used engineering material, the mechanical properties of titanium alloy under dynamic loads are closely related to their microstructure. In this work, the effects of solution treatment (ST) and solution and aging treatment (SAT) on the microstructure and dynamic compressive properties of Ti-6Al-4V alloy manufactured by selective laser melting were studied. The results showed that the microstructure of selective laser melted Ti-6Al-4V consisted of nearly full acicular α' martensite, then the acicular α' martensite was decomposed into α+β phase with basket-weave morphology with solution treatment. Clusters of α_2 particles with size of several hundred nanometers were precipitated in the α plates further with solution and aging treatment. The ultimate compressive strength (UCS) of selective laser melted TC4 alloy was increased with the increasing strain rate, showing strong strain rate hardening effect. Stress collapse happened once the strain exceeded 1500/s, which is the dominant failure model of selective laser melted TC4 under impacting load. As expected, the UCS of the ST sample decreased, but the ductility increased compared with the as-built sample; however, both the UCS and ductility of the SAT samples were enhanced synergistically due to the widely distributed α_2 precipitates. Besides, the SAT samples had the highest energy absorption compared with the as-built and ST counterparts under the same conditions, indicating that the SAT samples had better load-bearing capacities.

Keywords: Selective laser melting; Dynamic compressive properties; Ti-6Al-4V; Solution and aging treatment; Energy absorption.

1. Introduction

Nowadays, Ti-6Al-4V (TC4) alloy is a commonly used engineering material due to its combination of excellent mechanical properties, corrosion resistance and biocompatibility with low density, thus, it has attracted more attention in such fields as aeronautics and astronautics, automotive and marine engineering industries [1-3]. However, its poor machinability brings about serious problems, for example, the wasting ratio of material, long manufacturing time as well as difficulty in the fabrication of complex structures, which causes a significant increase of costs in the core devices in the aerospace field [4]. Hence, the growing market urgently needs a rapid response manufacturing method that can reduce the costs of aerospace devices. Selective laser melting (SLM), as one of the recently developed additive manufacturing techniques, emerged in the late 1980s and early 1990s [5, 6]. In this process, a high-density and focused laser beam is used to melt a thin layer of metallic powder in a "point-by-point and layer-by-layer" manner, which makes it able to directly fabricate dense metal parts with arbitrary complex structures [7]. Thus, the SLM parts are attracting more attention from both academic and engineering fields.

During the service period, it is highly likely that these additive manufactured parts are subjected to dynamic impacting loads, thus safety and stability become the major concerns. Take the widely reported bird-strike accident as example, the huge impacting force significantly damaged the aircraft structure and caused fatal accidents (in 15th January, 2009, a bird struck on an Airbus A320 belonging to American Airlines, the airplane crash-landed on the Hudson River because its engines failed to work after the bird-strike). Because the additive manufactured parts are being used more frequently in the aerospace field, they must possess high enough strength and impacting resistance to avoid dynamic damage failure under impacting loads. Recently, this has instigated interest into investigating the dynamic responses of additive manufactured parts, which has shown that the dynamic mechanical responses of the additive manufactured parts were different from those under quasi-static

conditions, namely the strain rate hardening effect [8-10].

As is commonly known, TC4 alloy is a typical dual-phase alloy because α and β phases can coexist at room temperature, thus the mechanical properties (especially dynamic mechanical properties) are highly dependent on its microstructure (i.e., fraction, morphology and distribution of α and β phases) [11]. Unlike the titanium alloy manufactured by traditional methods (e.g., casting and forging processes), the additive manufactured titanium is dominated by non-equilibrium and fine acicular martensite due to the extremely high heating and cooling rates [12]. It is widely accepted that the *hcp*-structure martensite phase is inherently brittle and responsible for low ductility, thus it cannot meet the requirement of core devices in the aerospace field [13]. Some researchers compared the dynamic compressive properties of additive manufactured TC4 alloy with the forged counterparts, the results showed that the former exhibited high strength but lower ductility [14]. Thus, some other researchers adopted post heating treatment to adjust and control the fraction and morphology of α and β phases to obtain comprehensive dynamic mechanical properties of the additive manufactured TC4 alloy [15, 16].

The aforementioned studies were mainly aimed to improve the mechanical properties of titanium alloy by heating it to the bi-phase interval and holding it for a while to promote the decomposition of martensite into stable α and β phases [17]. As is well known, titanium is an excellent high-temperature alloy, so it can be exposed to high temperature for a long time (e.g., the working temperature can reach as high as 600℃ in aircraft engine, which is equivalent to the aging temperature of titanium alloy) [18-20]. Consequently, nano-sized precipitates are bound to form under this condition, which will impose great influence on the strength and ductility of titanium alloy by dispersal reinforcing mechanism or load transfer mechanism [21]. However, researches on aging strengthening of additive manufactured titanium alloy are very limited to date, let alone studies on the effect of aging treatment on its microstructure and corresponding dynamic mechanical properties.

The aim of this work is to study the dynamic compressive properties of selective laser melted TC4 alloy under high strain rate impacting load. In order to obtain

comprehensive mechanical properties (including strength, ductility and energy absorption), microstructure the selective laser melted TC4 alloy was adjusted through different solution and aging treatments, which ensured a higher enough dynamic bearing capacities. This study provides a theoretical basis for the application of additive manufacturing technique in the extremely harsh service environment such as aerospace and marine engineering.

2. Experiment details

Gas atomized Ti-6Al-4V (TC4) alloy powder with spherical shape and mean particle size of 35μm was used in this work. Before the experiment, the powder was kept in an oven for 12 hours at 80℃ to remove moisture. A SLM apparatus (EOS M280) was adopted to manufacture the testing samples (5×5mm), the process parameters were determined as laser power of 280W, laser scan speed of 1200mm/s, layer thickness of 30μm and hatching space of 120μm. In order to prevent the samples from being oxidized during heating treatment, samples were sealed within quartz tubes filled with high-purity argon. These samples were heated to 955℃ (namely α+β treatment) with a fixed heating rate of 10℃/min and were kept for 1 hour before being cooled in air. Next, three groups of solution-treated samples were subjected to aging treatment for 8 hours at different aging temperature. The detail heat treatment regimes were shown in Fig. 1. Here, *T0* represented the room temperature (~25℃), *Ts* referred to the solution temperature (955℃) and *Ta* represents the aging temperature (515℃, 565℃ and 595℃).

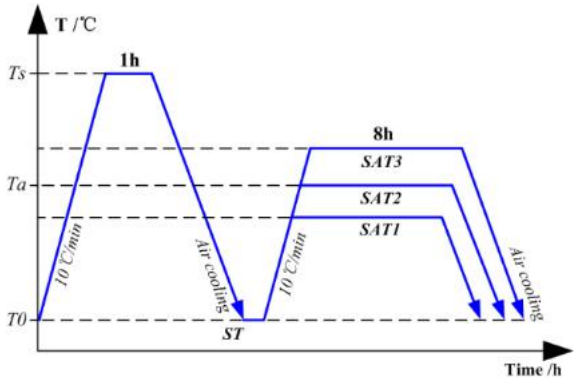

Fig. 1 The diagram of heating treatment regimes.

Phase analyse were conducted by X-ray diffraction (XRD) using D8 ADVANCE

X-ray diffractometer with Cu-K_α radiation operated at 40 kV and 40 mA with a step size of 0.02° and scanning speed 2°/min). Samples for microstructure characterization were prepared on the basis of standard metallographic procedures, and then etched in Kroll's solution (HF: HNO_3: H_2O=2: 4: 50) for 20s. Microstructure were observed by optical microscope (VHX-600), scanning electron microscope (Hitachi SU5000) and transmission electron microscope (JEM-2100). The sample for TEM observation were sliced as thin as 0.05mm, and then thinned by ion beam milling. Quasi-static compressive tests were performed on Zeiss Supra 55 FEG at velocity of 0.005mm/s, 0.05mm/s and 0.5mm/s, thus produced strain rates of 10^{-3}/s, 10^{-2}/s and 10^{-1}/s, respectively. High strain rate impacting tests were performed on a self-developed spit Hopkinson pressure bar (SHPB) testing system, as shown in Fig. 2. The loading direction was parallel to the building direction of the cylinder, while the striker bar was driven by nitrogen with different air pressures (0.08MPa, 0.2MPa, 0.3MPa, 0.4MPa, 1.0MPa), and thus produced strain rates of approximately 300/s, 900/s, 1200/s, 1500/s and 2400/s, respectively.

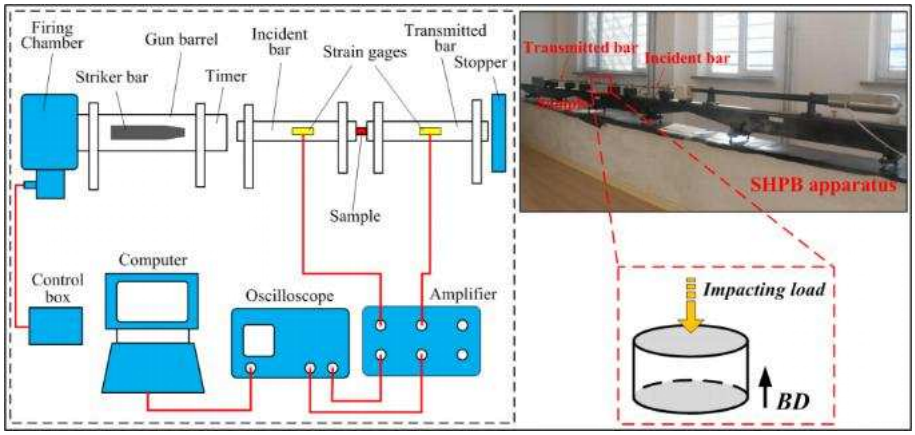

Fig.2 Schematic diagram and picture of spit Hopkinson pressure bar testing system.

The numerical solution was carried out by using ABAQUS/Explicit to obtain a deep understanding of dynamic mechanical responses of SLMed TC4 alloy, the numerical model of the SHPB testing was shown in Fig. 3. The model consisted three parts, namely incident bar, sample and transmitted bar, velocity load was applied on one end of the incident bar. In this study, the material of bars was 18Ni, which was considered as perfect elastic body to conduct the SHPB test, the material properties

were shown in Table 1. The dimensions of bars were ϕ14.5×1000mm, and those of sample were ϕ5×5mm. In order to reduce computational time, the bars and sample were meshed by C3D8R hexahedron elements with dimension size of 1.0mm and 0.1mm, respectively. Johnson-Cook model was used in the FE simulation, the parameters were listed in the Table 1, and the detail of the J-C model will be given in the section 3.3.2.

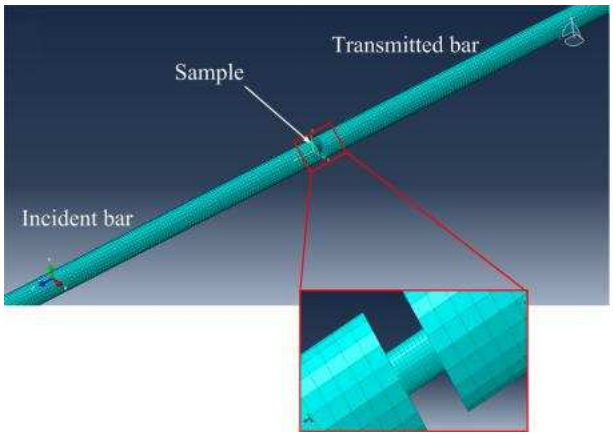

Fig. 3 The FE model of the SHPB testing.

Table 1 The material's parameters of bars and sample.

Item / Materials	Density (g/cm^3)	Young's Modulus (GPa)	Poisson's ratio
18Ni	7.8	190	0.3
Ti-6Al-4V	4.43	135	0.34

3. Results and discussion

3.1. Phase characterization

Fig. 4 showed the XRD patterns of the as-built, ST and SAT samples obtained in the diffraction angle 2θ ranged from 30° to 80°. Diffraction peaks of *hcp*-structure were detected in the as-built sample, which has been identified as α′ martensite in other literature [22]. Unlike the as-built sample, body centered cubic (*bcc*) of $(110)_\beta$ and $(200)_\beta$ diffraction peaks appeared at 2θ of ~39.5° and ~57.7° in the heat-treated counterparts, indicating that the α′ martensite has in-situ decomposed into stable α and β phases during heat treatments (in other study, the exact transformation is $\alpha' \rightarrow \alpha_s+\beta$ [23]). Moreover, it is worth to note that weak diffraction peaks at 2θ of ~64.3° were detected in the SAT samples, which corresponded to Ti_3Al (α_2) phase, indicating that

precipitate phase has been formed during the long-term aging process.

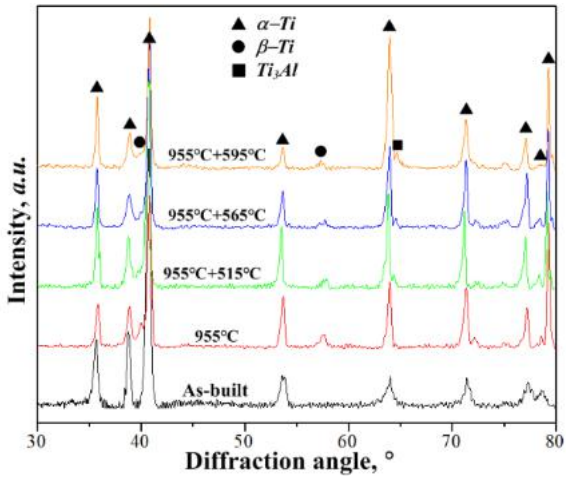

Fig. 4 XRD patterns of the as-built and heating-treated samples.

3.2. Microstructure

3.2.1. Microstructure of the as-built sample

Fig. 5 presented the optics and SEM micrographs from the top view of the as-built sample. The OM micrograph shows that no obvious pores were formed (Fig. 5a), and the high manufacturing quality implies the good mechanical properties of these parts. Moreover, Fig. 4b showed the bundles of equiaxed prior β grains, it was the result of alternating scanning manner and 66.7° shifting between adjacent layers during the SLM process, as shown in Fig. 5d. The SEM morphology exhibited in Fig. 5c shows that fine interlaced acicular α′ martensite with averaged width of 0.75±0.12μm was formed within these equiaxed prior β grains; the grain size and orientation were highly heterogeneous. It is commonly accepted that the *hcp*-structure martensite phase formed at a high cooling rate is inherently brittle and responsible for the high strength but low ductility in titanium alloy [13].

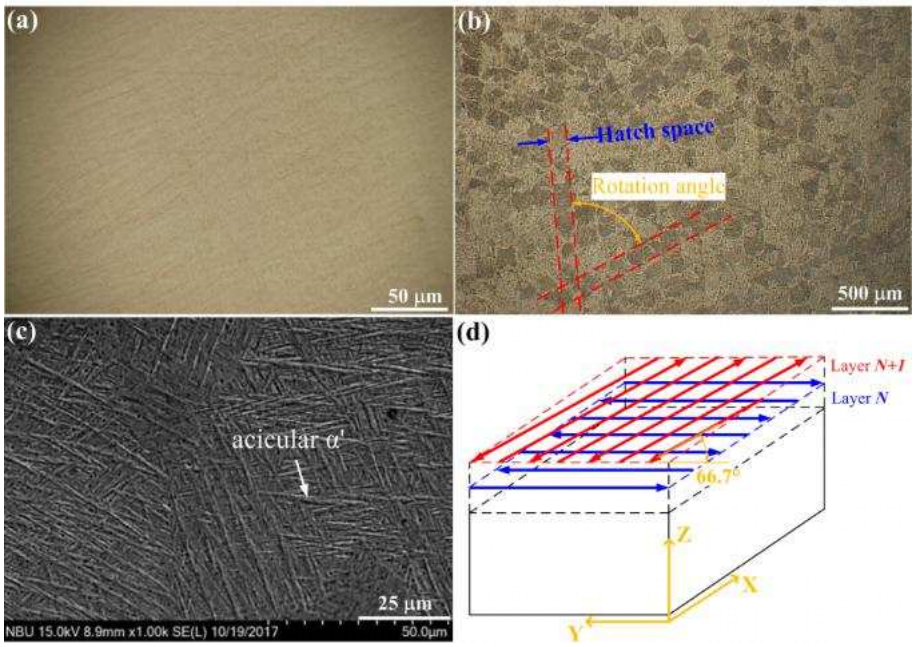

Fig. 5 Optics and SEM micrograph of the as-built TC4 alloy.

3.2.2. Microstructure of the heat-treated samples

Fig. 6 showed the optics micrographs of heat-treated samples, all of them presented basket-weave morphology with coarser α plates in the prior β grains. The OM micrograph of the ST sample shows that the continuous α grain boundaries (α_{GB}) have already broken down and started to globularize (as shown in the blue dashed lines in Fig. 6a). Some other researches also reported the globularization of α plates in the selective laser melted TC4 alloy after solution treatment [24,25], thus appropriate heating treatment regimes are expected to be attractive candidates to eliminate the microstructural and corresponding mechanical property anisotropy in additive manufactured parts. Fig. 6b-d showed the optical micrographs of the SAT samples. It can be seen that, except for the blurred boundary between α and β phases which makes the α plates difficult to identify, there was no remarkable change compared with the ST counterpart.

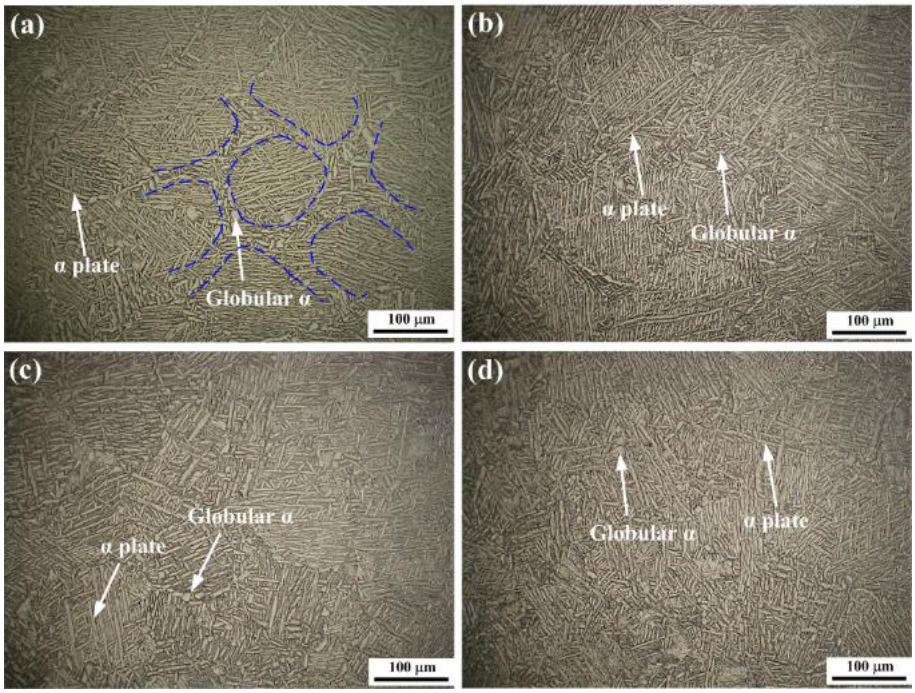

Fig. 6 Optical micrograghs of the heating-treated samples. (a) ST, (b) SAT1, (c) SAT2, (d) SAT3.

The SEM micrographs in Fig. 7 confirmed that the microstructure of the ST sample consisted of primary α plates with globular and plate-like morphology. A small amount of fine secondary α (α_s) was precipitated from the retained β grains, which formed a supersaturated β matrix. With aging treatment, the amount and size of the α_s increased significantly, this is because the subsequent aging treatment was able to provide enough driving force for the nucleation and growth of α_s phase during the long-term aging process. Moreover, due to the grain coarsening with heating treatment, the mean width of α plates of ST and SAT samples increased and the aspect ratio decreased significantly compared with the as-built counterpart (Fig. 5c). However, the width of α plates in SAT samples remained almost unchanged, while the aspect ratio decreased slightly compared to that of ST counterpart, this may be ascribed to the fact that the α plates split during the long-term aging process.

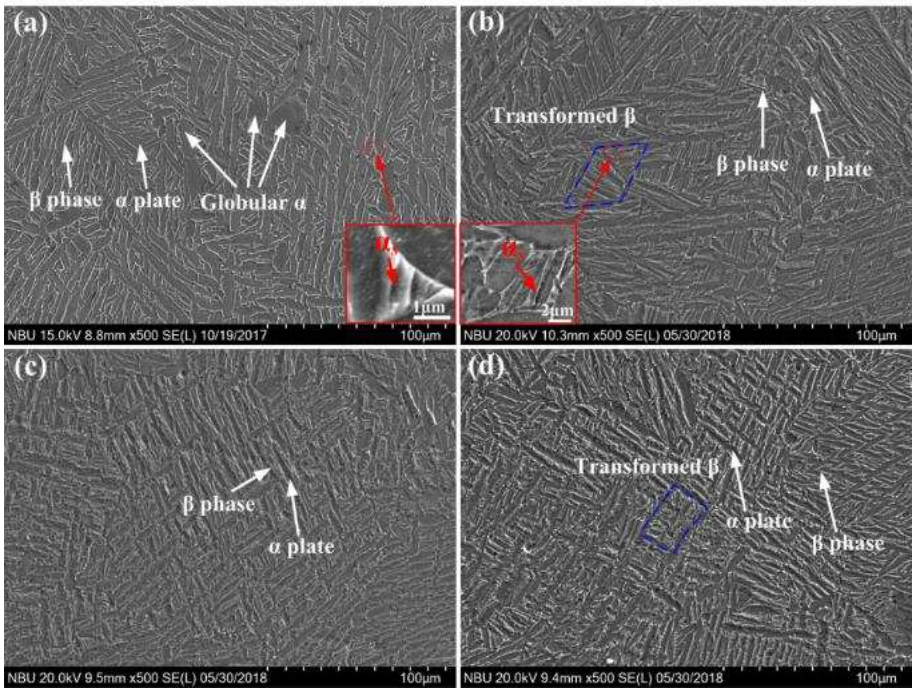

Fig. 7 SEM micrograghs of the heating-treated samples. (a) ST, (b) SAT1, (c) SAT2, (d) SAT3.

Higher magnified SEM micrographs were further obtained, as shown in Fig. 8. White particles with size of about 50-100nm were widely distributed in the α-Ti matrix in the SAT samples, while in the ST sample, very few white particles could be found. As illustrated in Fig. 8e, the EDS spectrum results showed that the white particle (point *B*) was characterized as Ti_3Al precipitate (known as α_2). The formation can be ascribed to the fact that the oversaturated vanadium atoms are expelled from the α phase during the long-term aging process, thus leading to higher aggregation of aluminum in it. When the content of aluminum surpasses the critical solid solubility of Ti_3Al, it starts to precipitate. Moreover, the solvus temperature of Ti_3Al decreases to around 500℃ as the content of aluminum is at relatively high level (wt. 7-9%) in TC4 alloy, aging at 500-600℃ is bound to promote the precipitation of Ti_3Al [23, 26]. This finding was consistent with the appearance of diffraction peaks of Ti_3Al in the XRD patterns (Fig. 4).

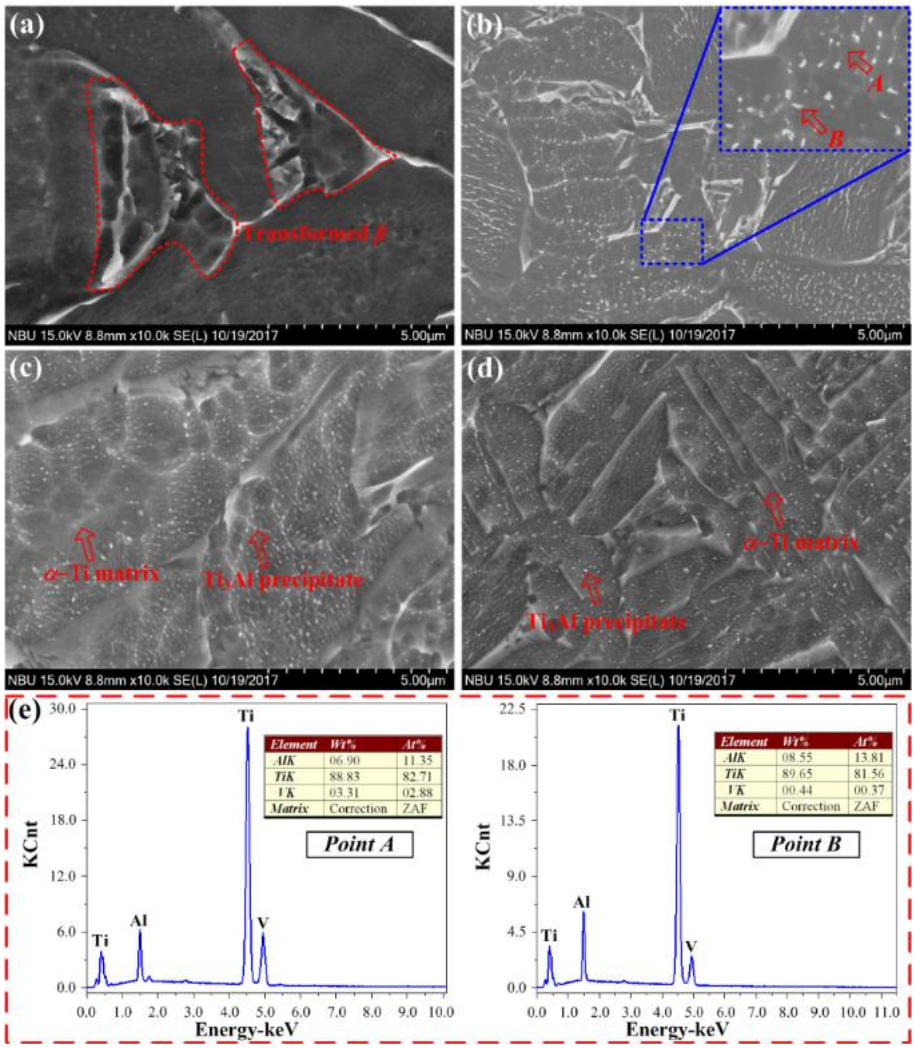

Fig. 8 Higher magnified SEM micrograghs of the heating-treated samples. (a) ST, (b) SAT1, (c) SAT2, (d) SAT3, (e) EDS spectrums taken from the measured points shown in (b).

In order to fully analyze the effect of heating treatment on the microstructure of selective laser melted TC4 alloy, TEM observations were conducted with the ST and SAT2 samples, as shown in Fig. 9. It can be seen from Fig. 9a that dense dislocation walls formed in the boundary of α/β, this may be attributed to the various thermodynamic properties of α and β phases. It is well known that thethermal expansion coefficient of α phase is much lower than that of β phase in dual titanium alloy [27], so great thermal stress is bound to concentrate in the boundary of α/β during the solution process, which would cause dense dislocations in the corresponding area. As for the dislocation lines in the α phase, these may be derived

from the dislocations from the primary α in the as-built sample. These dislocations will provide nucleation cores for the precipitated phase during the long-term aging process. As shown in Fig. 9c, the dislocations disappeared, and bundles of subcolonies of acicular α with average width of 300-500nm precipitated in the SAT2 sample, which can be ascribed to the re-nucleation in the primary α during the aging process. Moreover, clusters of Ti_3Al precipitate in these α-Ti matrix were observed, which was consistent with the finding in XRD and SEM observations. It was believed that the subcolony of acicular α, as well as the nano-sized α_2 particles, are favorable to improving the strength and ductility of TC4 alloy synergistically.

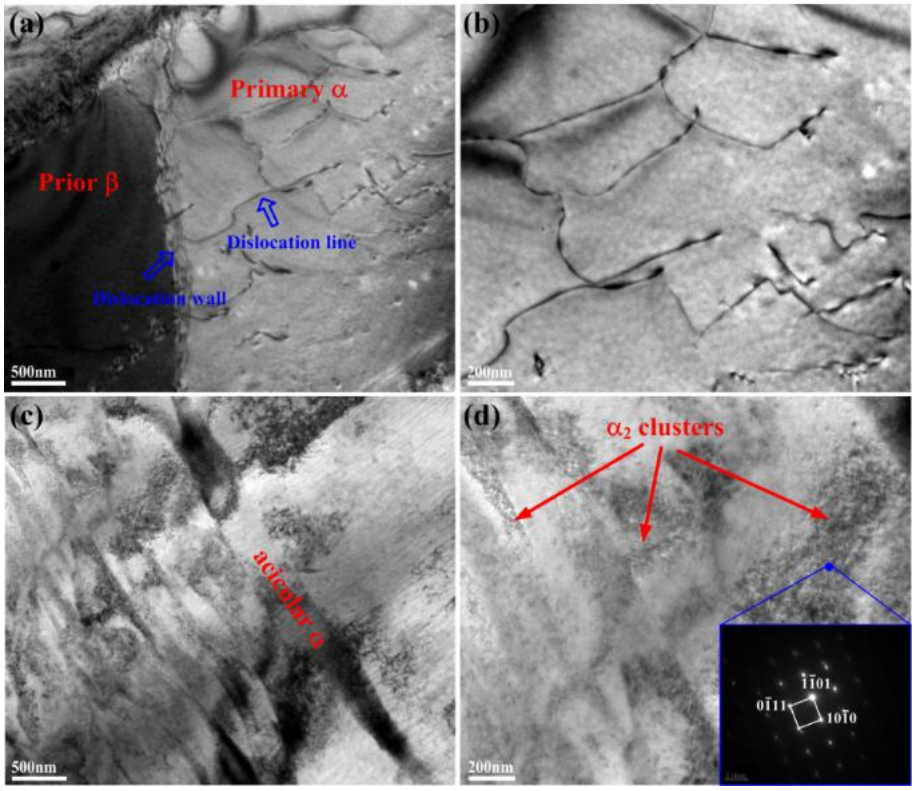

Fig. 9 Bright-field TEM micrograghs of ST sample (a, b) and SAT2 sample (c, d).

3.3. Dynamic compressive properties of the TC4 alloy

3.3.1 dynamic properties of the as-built parts

Fig. 10 presented the stress-strain curves of the as-built sample at different compressive strain rates. It can be seen from Fig. 10a that curves in the elastic deformation region changed a little as the strain rate varied within the quasi-static loading range (10^{-3} to 10^{-1}/s); the corresponding elastic modulus was about 135GPa. As the strain rate increased into the dynamic impacting range (300-2400/s), the elastic

modulus increased to 215GPa, Wang et al. also found that the elastic modulus of TC16 alloy changed a lot under quasi-static and dynamic loads, respectively [28]. As shown in Fig. 10b, it is interesting to note that the samples tested at a quasi-static and lower strain rate (less than 1200/s) loads exhibited a certain strain hardening effect, the ultimate compressive strength (UCS) appeared at the state of unloading. However, when the strain rate reached higher value (more than 1200/s), the compressive strength reached the climax at the beginning stage of plastic deformation. Moreover, the UCS values increased slightly from 1298MPa to 1340MPa as the strain rate varied within the quasi-static loading range (10^{-3}-10^{-1}/s), then it increased significantly from 1388MPa to 1627MPa once the strain rate increased into the dynamic impacting range (300-2400/s), showing obvious strain rate hardening effect of the selective laser melted TC4 alloy.

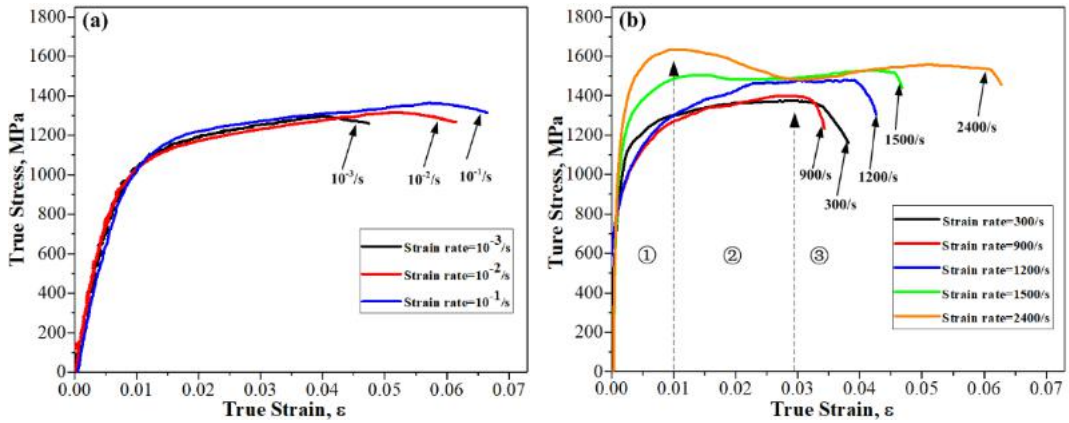

Fig. 10 Compressive stress-strain curves of the as-built sample. (a) Tested at quasi-static load, (b) tested at dynamic load.

As illustrated in Fig. 11, the authors compared the compressive properties of TC4 alloy manufactured by different additive manufacturing techniques to quantitatively evaluate the relationship between strain rate and mechanical properties of the AM TC4 alloy. It can be seen that at relatively low strain rate (10^{-3}-10^{0}/s), the slope of fit line was much smaller than that that at relatively high strain rate, indicating that strain rate hardening effect became more distinct at high strain rate than that at low strain rate, the same trend was also drawn by Li et al. [32].

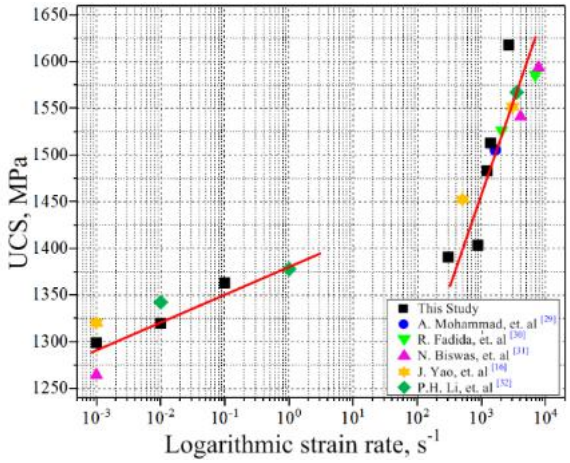

Fig. 11 Function of UCS versus strain rate plot for additive manufactured TC4 alloy.

3.3.2 The constitutive model and simulation

In engineering, many thermo-visco plastic constitutive models were frequently applied to depict the mechanical properties under different loading conditions, for example, the Johnson-Cook model [33], Zerrilli-Armstrong model [34] and Chang-Asaro model [35], etc. Among them, the Johnson-Cook (J-C) model not only has simple mathematical expression, but also is suitable for materials of various crystal structures and large deformation. Thus, the J-C model was applied to describe the constitutive of the SLMed Ti-6Al-4V alloy in this study, which can be expressed as:

$$\sigma = (A + B\varepsilon^{n})\left[1 + C\ln\left(\frac{\dot{\varepsilon}}{\dot{\varepsilon}_0}\right)\right]\left[1 - \left(\frac{T - T_0}{T_m - T_0}\right)^{m}\right]$$

The three brackets depict the work hardening effect, strain rate hardening effect and thermal softening effect, respectively. In this study, all the tests were performed at reference temperature (~25℃), thus the effect of temperature (exponent m) was ignored. The σ is the (Von Mises) flow stress (MPa), A is the yield stress (MPa) at reference temperature and reference strain rate, B is the coefficient of strain hardening (MPa), n is the strain hardening exponent. The A, B and n were determined at the reference strain rate, which resulted in A=1032MPa, B=1301MPa and n=0.466. Regarding the strain rate effect (the second bracket), the $\dot{\varepsilon}$ is the strain rate and $\dot{\varepsilon}_0$ is the reference strain rate (10^{-3}/s). C is the material constants that represent the

coefficient of strain rate hardening, which was fit at different strain rates, resulting into C=0.009. Then, the J-C constitutive model of SLMed Ti-6Al-4V alloy under impacting loads was determined as:

$$\sigma = (1032 + 1301\varepsilon^{0.466})\left[1 + 0.009\ln\left(\frac{\dot{\varepsilon}}{\dot{\varepsilon}_0}\right)\right]$$

Then, FEM simulations were performed at strain rates of 300/s, 1200/s, 1500/s and 2400/s, the results were showed in Fig. 12. It can be seen that at relatively low strain rates (300/s and 1200/s), the simulation results were in good agreement with the experimental results, while there was large deviation at relatively high strain rates (1500/s and 2400/s), especially at low strain, which can be attributed to the stress collapse occurred at 1500/s and 2400/s (which will be discussed next). Because the parameter C was fitted by using the data that eliminated the oscillation data at high strain rates, so the simulation result failed to be consistent with the experimental result at low strain section.

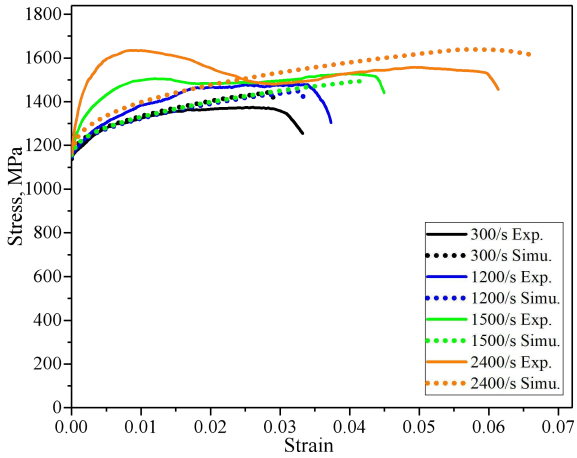

Fig. 12 Comparing between the experimental and simulation results based on the J-C model.

It was worth to note that stress collapse happened at strain about 1% the samples at strain rates of 1500/s and 2400/s. At the beginning stage, compressive strength increased rapidly with the increase of strain and reached the peak value at strain of about 1.0% (stage ①). At the next stage, the compressive strength decreased rapidly with the increase of strain to 2.8% (stage ②). In the final dynamic equilibrium stage, the compressive strength remained almost unchanged as the strain increased until

unloading, and thus formed a platform at about 1400MPa (stage ③). The FEM results illustrated that when the SLMed TC4 alloy was tested at strain rate of 300/s, flow stress was concentrated in the core area of part, the maximal flow stress was 1355MPa (Fig. 13a). When the strain rate increased to 1200/s, flow stress increased to 1500MPa, showing obvious strain rate hardening effect. Moreover, the stress not only concentrated in the core area of part, but also formed concentrated bands along the diagonal directions, as indicated by the dash lines (Fig. 13b). However, the degree of stress concentration was slight, implying that stress collapse may still in its initial stage.

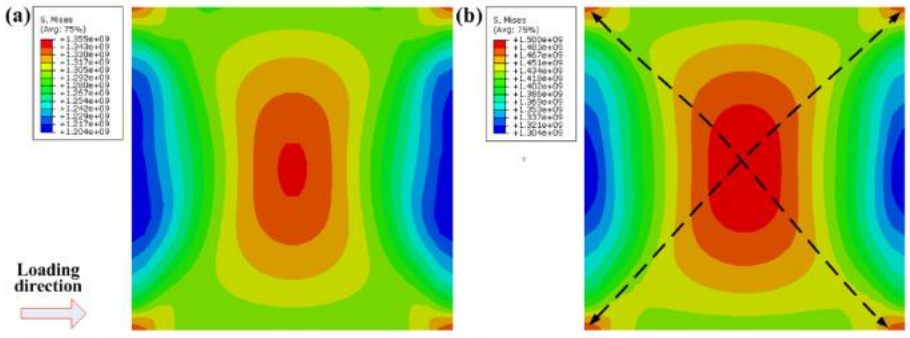

Fig. 13 The contour plots of stress in the as-built TC4 alloy tested at strain rates of (a) 300/s and (b) 1200/s at the moment before rupture.

In the FE simulation at strain rate of 2400/s, the moment that the incident bar hit the sample was set as 0μs, it can be seen that the maximum flow stress increased to 1616MPa in only 12μs, as shown in Fig. 14a and b (corresponding to the ① stage in Fig. 10b). However, the stress in the core area turn to decrease immediately even the maximum flow stress keep increasing to 1654MPa, indicating that stress collapse started to happen, as shown in Fig. 14c-e (corresponding to the ② stage in Fig. 10b). The occurrence of stress collapse represented the generation of adiabatic shear bands (ASBs), which are regarded as the dominant failure mode for alloy with lower thermal conductivity and a higher thermal softening rate (e.g. TC4 alloy) under high strain rate load [36, 37]. ASBs are more likely to develop along the direction of maximum stress due to the serious plastic deformation, it was accepted that no more than 10% of the plastic work can be stored as the internal energy while the other generates heat [16]. Some researches have been devoted to study the internal heat generation within

the ASBs [38,39], in these studies, the effects of macro stress, strain, strain rate and their coupling relationships on the formation of ASBs were concerned. During the dynamic loading, the deformation process is within several microseconds (~80μs), the heat has no enough time to dissipate to surroundings and thus leads to the increase of sample temperature consequentially. The increasing temperature will accelerate the process of thermoviscoplastic constitutive instability, which causes the deformation of material to be highly localized. In the stage ③, the competition between thermal softening and strain hardening effects reached to the dynamic equilibrium state, and made the curve relative flat until rupture. In this stage, the ASBs developed along the stress concentration direction, and then developed into cracks. The cracks continue to develop along the diagonal directions, as shown in Fig. 14f-h, which lead to the final rupture at about 68μs (corresponding to the ③ stage in Fig. 10b).

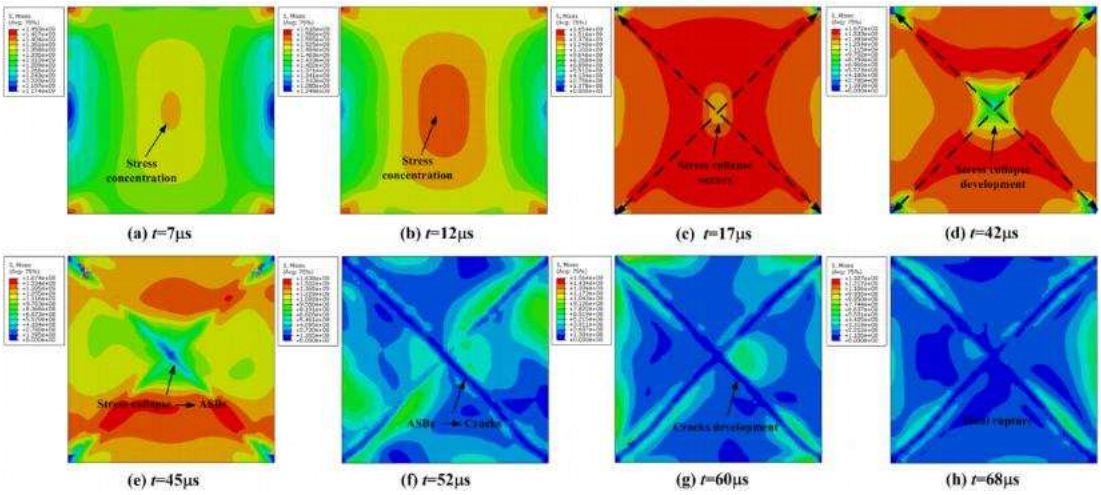

Fig. 14 The evolution of stress in the as-built TC4 alloy tested at strain rate of 2400/s. (a, b) stage ①, (c-e) stage ②, (f-h) stage ③.

3.3.3 Dynamic properties of the heat-treated parts

Fig. 15a showed the stress-strain curves of ST and SAT samples at compressive strain rates of about 1500/s. We can see that the solution treatment brought about great influence on the dynamic compressive properties of the selective laser melted TC4 alloy compared with the as-built counterpart. As expected, once tested at strain rate of 1500/s, the as-built sample had higher UCS (1495MPa) but smaller strain to unloading (3.9%), while the ST sample exhibited lower UCS (1425MPa) but higher

strain to unloading (8.5%). These variations in dynamic compressive properties reflected the difference of microstructure and phase in the as-built and ST samples, as demonstrated by the fact that finer grain conduces to higher strength and β phase conduces to the ductility in titanium alloy, as illustrated in Fig. 5 and 6. The same conclusion was also illustrated by other reports [40, 41].

Regarding the SAT samples, the values of UCS and strain of SAT1, SAT2 and SAT3 increased to 1535MPa and 11.8%, 1505MPa and 9.8% and 1590MPa and 11.7% under the same conditions, respectively, showing obvious synergistic effect of reinforcing and toughening compared with the as-built and ST counterparts. It can be seen that the biggest difference between the ST and SAT samples lies in the nano-sized α_2 precipitates (as illustrated in Fig. 8), which should be responsible for the discrepancies of dynamic compressive properties between the ST and SAT samples. On one hand, the coarsening grains increased the ductility of the ST sample; on the other hand, the existence of α_2 particles enhanced the strength of the SAT samples by the load transfer mechanism without reducing the ductility. As shown in Fig. 15b, when the strain rate increased to 2400/s, all the tested samples (including the as-built, ST and SAT samples) were fractured. The UCS values of as-built and ST samples increased by 134MPa and 166MPa, respectively, but that of the SAT samples increased by less than 100MPa. This is because the widely distributed α_2 particles were able to transfer the impacting load efficiently in several milliseconds, and thus led to lower sensitivity to the strain rate of the SAT samples.

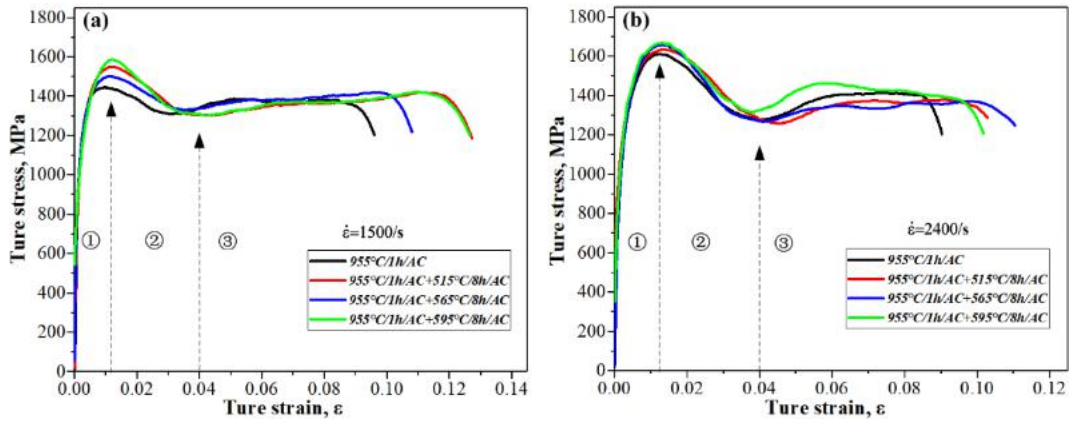

Fig. 15 Stress-strain curves of the heat-treated samples tested at strain rates of (a) 1500/s and (b) 2400/s.

In this study, the samples tested at strain rate of 2400/s ruptured completely, while those tested at strain rates below 2400/s maintained integrity after testing. Fig. 16 showed the SEM micrographs of fracture surfaces of the as-built, ST and SAT2 samples at strain rate of 2400/s. All the fracture surfaces were flat and were almost 45° to the loading axis, which can be characterized as typical shearing fracture pattern. Fig. 16a and b presented the fracture surface of the as-built sample, the lower magnification image showed that most area was smooth, only very small area of dimple can be observed. The higher magnification image showed that the dimple was small and shallow. Fig. 16c and d showed the fracture surface of the ST sample, both dimple and smooth areas were distributed alternately on the whole fracture surface, moreover, the area of dimple increased comparing with the as-built sample. Fig. 16e and f exhibited the fracture surface of the SAT2 sample, the percentage of dimple area increased significantly comparing with the as-built and ST samples, the size and depth of the dimple became a little bit bigger, indicating that the SAT sample had better plasticity. Moreover, elongated dimples were found in the ST and SAT samples, which is the evident of failure by shear stress. It is widely accepted that the dimple area exhibits ductile fracture characteristic, while smooth area usually exhibits brittle fracture characteristic. This is consistent with the fact that the fracture occurring in adiabatic shear bands is not uniform, and ultimate ruptures resulted from ductile and brittle fracture modes [16].

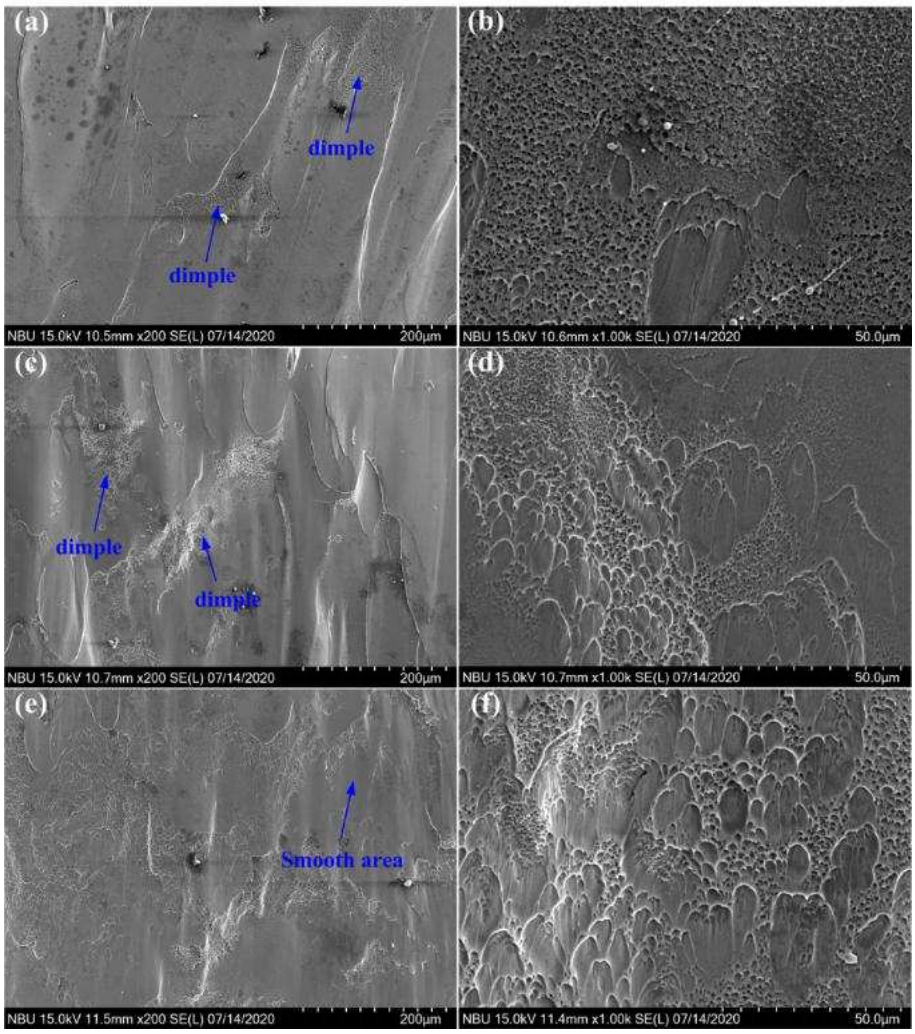

Fig. 16 Fracture morphologies of TC4 alloy at strain rate of 2400/s. (a, b) As-built sample, (c, d) ST sample, (e, f) SAT2 sample.

3.3.4 Energy absorption of the SLMed TC4 alloy

It was estimated that about 10% of the impacting work can transfer into internal energy of the tested part [16], while the rest will dissipate or transfer into heat. If the heat generation rate is larger than the dissipating rate, the temperature of the tested part will increase correspondingly. Obviously, the stored energy is bound to impose important effects on the impacting process, so absorption energy was calculated in this section, which can be characterized as $E = \int_0^{\varepsilon} \sigma d\varepsilon$, here [0,ε] represents the strain in a certain range [42]. As mentioned, although the TC4 alloy still had high stress even though stress collapse happened, it is an unstable state and no longer suitable for engineering application. Because of this, the energy absorption of a material should be

measured prior to stress collapse, as shown in Fig. 12 (stage ① and ②).

Fig. 17 shows the energy absorption of the as-built, ST and SAT samples at strain rates of 1500/s and 2400/s; as expected, the energy absorption of all the samples increased with the increasing strain rate, however, it was found that the as-built sample had the largest increment, while the ST and SAT samples had relatively smaller increment. This may be due to the fact that the ASB in the as-built sample at strain rate of 1500/s was in its initial stage of formation (as illustrated by the peaks of stress collapse), while the ASBs in the ST and SAT samples at strain rate of 1500/s had already been in their middle or even later stages.

At strain rate of 2400/s, energy absorption of the as-built sample was 49.2kJ/m^3, but increased to 54.6kJ/m^3 for the ST sample; this is because the ST sample had good deformation coordination caused by the globular α phase [24]. With regard to the SAT samples, energy absorption further slightly increased to 58.0kJ/m^3, 56.8kJ/m^3 and 58.4kJ/m^3 for the SAT1, SAT2 and SAT3 samples, respectively. This is due to the fact that the nano-sized α_2 precipitates are conducive to improving the load-bearing capacity of TC4 alloy under a dynamic compressive load. In practice, higher energy absorption means higher damping properties [20], which is conducive to absorbing more vibration and oscillation of the core devices in the fields of aerospace and marine engineering, and others, hence, resonance can be prevented efficiently.

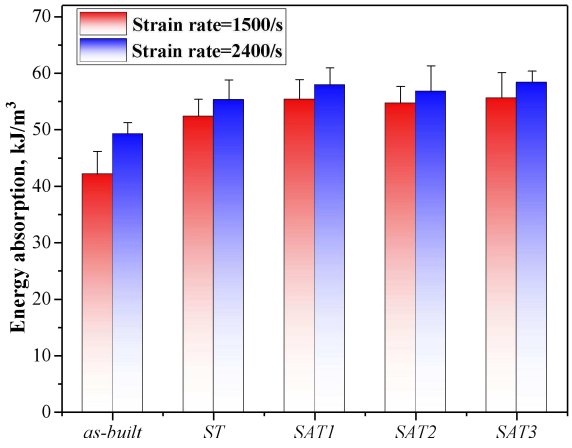

Fig. 17 Energy absorption (before the stress collapse) of the as-built, ST and SAT samples at strain rates of 1500/s and 2400/s.

4. Conclusions

In this work, the effects heat treatment on the microstructure and dynamic compressive properties of selective laser melted Ti-6Al-4V alloy were systematically studied, the following conclusions can be drawn.

(1) Once subjected to solution treatment, acicular α' martensite in the selective laser melted TC4 alloy was transformed into α+β phase with globular and plate-like morphology. With solution and aging treatment, although the morphology changed a little, clusters of α_2 particles with sizes of several hundred nanometers were precipitated in the α plates.

(2) The selective laser melted TC4 alloy exhibited obvious strain rate hardening effect. As the strain rate increased from 10^{-3}/s to 2400/s, the UCS was increased from 1298MPa to 1627MPa. Moreover, stress concentrated in the core area of part at lower strain rate, while at higher strain rate, adiabatic shear bands formed and thus caused stress collapse.

(3) The microstructure and phase affected the dynamic mechanical responses significantly. Comparing with the as-built sample, the compressive strength of the ST sample decreased but the ductility increased. However, both the compressive strength and ductility of the SAT samples were enhanced due to the widely distributed α_2 precipitates. Besides, the SAT samples had higher energy absorption, indicating that the SAT samples had better load-bearing capacities.

Acknowledgement

This work was supported by the Natural Science Foundation of China (Grant No. 51905279, 11972202); National Key Laboratory of Shockwave and Detonation Physics (Grant No. 6142A0320102); Science Challenge Project (Grant No. TZ2018001); Foundation of Key Laboratory of Impact and Safety Engineering, Ministry of Education (Grant No. CJ201913); Major Projects of Scientific & Technological Innovation (2025) of Ningbo City (Grant No. 2018B10007). Yang Liu wishes to thank the China Scholarship Council for the award to study at Cardiff University (Grant No. 201808330129). The authors would also like to acknowledge the supports from the ASTUTE 2020 (Advanced Sustainable Manufacturing Technologies). The operation, supporting manufacturing companies across Wales, has

been part-funded by the European Regional Development Fund through the Welsh Government and the participating Higher Education Institutions.

References

[1] H. Shipley, D. McDonnell, M. Culleton, R. Coull, R. Lupoi, G. O'Donnell, D. Trimble. Optimization of process parameters to address fundamental challenges during selective laser melting of Ti-6Al-4V: A review. Int. J. Mach. Tool. Manu. 128 (2018) 1-20.

[2] Q.Q. Han, R. Setchi, S.L. Evans. Synthesis and characterisation of advanced ball-milled Al-Al_2O_3 nanocomposites for selective laser melting. Powder Technol. 297 (2016) 183-192.

[3] K.J. Lin, L.H. Yuan, D.D. Gu. Influence of laser parameters and complex structural features on the bio-inspired complex thin-wall structures fabricated by selective laser melting. J. Mater. Process. Tech. 267 (2019) 34-43.

[4] S.M. Thompson, Z.S. Aspin, N. Shamsaei, A. Elwany, L. Bian. Additive manufacturing of heat exchangers: A case study on a multi-layered Ti-6Al-4V oscillating heat pipe. Addit. Manuf. 8 (2015) 163-174.

[5] J.L. Zhang, B. Song, Q.S. Wei, D. Bourell, Y.S. Shi. A Review of Selective Laser Melting of Aluminum Alloys: Processing, Microstructure, Property and Developing Trends. J. Mater. Sci. Technol. 35 (2019) 270-284.

[6] Y. Liu, J. Zhang, Z.C. Pang. Numerical and experimental investigation into the subsequent thermal cycling during selective laser melting of multi-layer 316L stainless steel. Opt. Laser Technol 98 (2018) 23-32.

[7] C.H. Song, A.M. Wang, Z.J. Wu, Z.Y. Chen, Y.Q. Yang, D. Wang. The design and manufacturing of a titanium alloy beak for Grus japonensis using additive manufacturing. Mater. Design 117 (2017) 410-416.

[8] S.H. Riza, S.H. Masood, C. Wen, D. Ruan, S.Q. Xu. Dynamic behaviour of high strength steel parts developed through laser assisted direct metal deposition. Mater. Des. 64 (2014) 650-659.

[9] I. Rosenthal, A. Stern, N. Frage. Strain rate sensitivity and fracture mechanism of AlSi10Mg parts produced by Selective Laser Melting. Mater. Sci. Eng A 682 (2017)

509-517

[10] R. Bobbili, V. Madhu. Effect of strain rate and stress triaxiality on tensile behavior of titanium alloy Ti-10-2-3 at elevated temperatures. Mater. Sci. Eng. A 667 (2016) 33-41.

[11] J.J. Yang, H.C. Yu, J. Yin, M. Gao, Z.M. Wang, X.Y. Zeng. Formation and control of martensite in Ti-6Al-4V alloy produced by selective laser melting. Mater. Design 108 (2016) 308-318.

[12] J.H. Yao, Y. Wang, G.L. Wu, M. Sun, M. Wang, Q.L. Zhang. Growth characteristics and properties of micro-arc oxidation coating on SLM-produced TC4 alloy for biomedical applications. App. Surf. Sci. 479 (2019) 727-737.

[13] J. Haubrich, J. Gussone, P.B. Vila, P. Kürnsteiner, E.A. Jagle, D. Raabe, N. Schell, G. Requena. The role of lattice defects, element partitioning and intrinsic heat effects on the microstructure in selective laser melted Ti-6Al-4V. Acta Mater. 167 (2019) 136-148.

[14] W.W. Ming, J. Chen, Q.L. An, M. Chen. Dynamic mechanical properties and machinability characteristics of selective laser melted and forged Ti6Al4V. J. Mater. Process. Technol. 271 (2019) 284-292.

[15] Y. Liu, Z.C. Pang, M. Li, Y.G. Wang, D. Wang, C.H. Song, S.X. Li. Investigation into the dynamic mechanical properties of selective laser melted Ti-6Al-4V alloy at high strain rate tensile loading. Mater. Sci. Eng. A 745 (2019) 440-449.

[16] J. Yao, T. Suo, S.Y. Zhang, F. Zhao, H.T. Wang, J.B. Liu, Y.Z. Chen, Y.L. Li. Influence of heat-treatment on the dynamic behavior of 3D laser deposited Ti-6Al-4V alloy. Mater. Sci. Eng. A 677 (2016) 153-162.

[17] Z.L. Liang, Z.G. Sun, W.S. Zhang, S.K. Wu, H. Chang. The effect of heat treatment on microstructure evolution and tensile properties of selective laser melted Ti6Al4V alloy. J. Alloy. Compd. 782 (2019) 1041-1048.

[18] Z.C. Fan, H.W. Feng. Study on selective laser melting and heat treatment of Ti-6Al-4V alloy. Results Phys. 10 (2018) 660-664.

[19] M. Muhammad, J.W. Pegues, N. Shamsaei, M. Haghshenas. Effect of heat

treatments on microstructure/small-scale properties of additive manufactured Ti-6Al-4V. Int. J. Adv. Manuf. Tech. 103 (2019) 4161-4172.

[20] D.G. Lee, S. Lee, Y.T. Lee. Effect of precipitates on damping capacity and mechanical properties of Ti-6Al-4V alloy. Mat. Sci. Eng. A 486 (2008) 19-26.

[21] A. Radecka, J. Coakley, V.A. Vorontsov, T.L. Martin, P.A.J. Bagot, M.P. Moody, D. Rugg, D. Dye. Precipitation of the ordered α_2 phase in a near-α titanium alloy. Scripta Mater. 117 (2016) 81-85.

[22] B. Vrancken, L. Thijs, J.P. Kruth, J.V. Humbeeck. Heat treatment of Ti6Al4V produced by Selective Laser Melting: Microstructure and mechanical properties. J. Alloy. Compd. 541 (2012) 177-185.

[23] J. Wang, X. Lin, M. Wang, J.Q. Li, C. Wang, W.D. Huang. Effects of subtransus heat treatments on microstructure features and mechanical properties of wire and arc additive manufactured Ti-6Al-4V alloy. Materials Science & Engineering A 776 (2020) 139020

[24] Z. Zhao, J. Chen, H. Tan, G.H. Zhang, X. Lin, W.D. Huang. Achieving superior ductility for laser solid formed extra low interstitial Ti-6Al-4V titanium alloy through equiaxial alpha microstructure. Scripta Mater. 146 (2018) 187-191.

[25] R. Sabban, S. Bahl, K. Chatterjee, S. Suwas. Globularization using heat treatment in additively manufacturedTi-6Al-4V for high strength and toughness. Acta Mater. 162 (2019) 239-254.

[26] D. Lunt, T. Busolo, X. Xu, J.Q. Fonseca, M. Preuss. Effect of nanoscale α_2 precipitation on strain localisation in a two-phase Ti-alloy. Acta Mater. 129 (2017) 72-82.

[27] R. Shi, Z.H. Nie, Q.B. Fan, F.C. Wang, Y. Zhou, X. Liu, Correlation between dislocation-density-based strain hardening and microstructural evolution in dual phase TC6 titanium alloy. Mater. Sci. Eng. A 715 (2018) 101-107.

[28] Y. Yang, B.F. Wang. Microstructure evolution in adiabatic shear band in alpha-titanium. J. Mat. Sci. 41(22) 2006 7387-7392.

[29] A. Mohammad, S.H. Masood1, D. Fraser, M. Jahedi. Dynamic compressive behaviour of Ti-6Al-4V alloy processed by electron beam melting under high strain

rate loading. Adv. Manuf. 3 (2015) 232-243.

[30] R. Fadida, D. Rittel, A. Shirizly. Dynamic mechanical behavior of additively manufactured Ti6Al4V with controlled voids. J. Appl. Mech. 82 (2015) 041004.

[31] N. Biswas, J.L. Ding, V.K. Balla, D.P. Field, A. Bandyopadhyay. Deformation and fracture behavior of laser processed dense and porous Ti6Al4V alloy under static and dynamic loading. Mat. Sci. Eng. A 549 (2012) 213-221.

[32] P.H. Li, W.G. Guo, W.D. Huang, Y. Su, X. Lin, K.B. Yu. Thermomechanical response of 3D laser-deposited Ti–6Al–4V alloy over a wide range of strain rates and temperatures. Mat. Sci. Eng. A 647 (2015) 34-42.

[33] Y.H. Zhao, J. Sun, J.F. Li, Y.Q. Yan, P. Wang. A comparative study on Johnson-Cook and modified Johnson-Cook constitutive material model to predict the dynamic behavior laser additive manufacturing FeCr alloy. J. Alloy. Compd. 723 (2017) 179-187.

[34] C. Baxter, E. Cyr, A. Odeshi, M. Mohammadi. Constitutive models for the dynamic behaviour of direct metal laser sintered AlSi10Mg_200C under high strain rate shock loading. Mat. Sci. Eng. A 731 (2018) 296-308.

[35] R. Alaghmandfard, D. Chalasani, A. Hadadzadeh, B.S. Amirkhiz, A. Odeshi, M. Mohammadi. Dynamic compressive response of electron beam melted Ti–6Al–4V under elevated strain rates: Microstructure and constitutive models. Addi. Manuf. 35 (2020) 101347.

[36] F. Martinez, L.E. Murr, A. Ramirez, M.I. Lopez, S.M. Gaytan. Dynamic deformation and adiabatic shear microstructures associated with ballistic plug formation and fracture in Ti-6Al-4V targets. Mater. Sci. Eng. A 454-455 (2007) 581-589.

[37] A.G. Odeshi, S. Alameeri, M.N. Bassim, Effect of high strain rate on plastic deformation of a low alloy steel subjected to ballistic impact. J. Mater. Process. Technol. 162-163 (2005) 385-391.

[38] Z. Zhang, Daniel E. Eakins, Fionn P.E. Dunne. On the formation of adiabatic shear bands in textured HCP polycrystals. Int. J. Plast., 79 (2016) 196-216.

[39] Y. Chen, S. Ghosh. Micromechanical analysis of strain rate-dependent

deformation and failure in composite microstructures under dynamic loading conditions. Int. J. Plast., (32-33) 2012 218-247.

[40] A. Zafaria, M.R. Barati, K. Xia. Controlling martensitic decomposition during selective laser melting to achieve best ductility in high strength Ti-6Al-4V. Mater. Sci. Eng. A 744 (2019) 445-455.

[41] X.C. Yan, S. Yin, C.Y. Chen, C.J. Huang, R. Bolot, R. Lupoi, M. Kuang, W.Y. Ma, C. Coddet, H.L. Liao, M. Liu. Effect of heat treatment on the phase transformation and mechanical properties of Ti6Al4V fabricated by selective laser melting. J. Alloy. Compd. 764 (2018) 1056-1071.

[42] Z.C. Pang, Y. Liu, M. Li, C.L. Zhu, Y.G. Wang, S.X. Li, D. Wang, C.H. Song. Influence of process parameter and strain rate on the dynamic compressive properties of selective laser melted Ti-6Al-4V alloy. Appl. Phys. A 125 (2019) 90.